Published in Applied Physics Letters 91, issue 111115, 1-3, 2007
which should be used for any reference to this work

InGaAs/AlAsSb quantum cascade detectors operating in the near infrared

F. R. Giorgetta,[a] E. Baumann, and D. Hofstetter
Institute of Physics, University of Neuchâtel, Neuchâtel CH-2000, Switzerland

C. Manz, Q. Yang, and K. Köhler
Fraunhofer Institute for Applied Solid State Physics, Freiburg, D-79108, Germany

M. Graf
Institute for Microstructural Sciences, National Research Council, Ottawa K1A 0R6, Canada

The authors report on short-wavelength $In_{0.53}Ga_{0.47}As/AlAs_{0.56}Sb_{0.44}$ quantum cascade detectors (QCDs). At room temperature, one device detects at 505 meV (2.46 μm) with a responsivity of 2.57 mA/W, while a second QCD is sensitive at 580 meV (2.14 μm) with a responsivity of 0.32 mA/W.

With the recent development and commercialization of quantum cascade lasers, fast and sensitive semiconductor-based detectors for the mid-to far-infrared wavelength range are rapidly becoming key components for future optical sensor systems. The photoconductive quantum well infrared photodetector (PC-QWIP) is certainly the most mature device for these wavelengths. Almost in parallel to the development of the PC-QWIP, photovoltaic QWIPs (PV-QWIPs) have been proposed and fabricated. The pioneering works of Schneider *et al.*[1] and Levine *et al.*[2] have paved the way for a thorough understanding of this device. Yet another version of the PV-QWIP, namely the quantum cascade detector[3] (QCD), has recently experienced substantial progress. Similar to the PV-QWIPs, these devices have the advantage that no external bias voltage is necessary for operation, leading to zero dark current and a favorable noise behavior. QCDs were reported at 5, 9, 17, and 84 μm (Refs. 4–7) and have been fabricated using either InGaAs/InAlAs or AlGaAs/GaAs. Shorter operation wavelengths are however difficult to obtain with those semiconductor materials due to their relatively low conduction band offsets (CBOs) of 0.5 eV (InGaAs/InAlAs) and 1 eV, respectively, (AlAs/GaAs). An alternative system making the wavelength range between 2 and 3 μm available for QCDs is the InGaAs/AlAsSb lattice matched to InP; this combination offers a CBO of 1.6 eV,[8] which is theoretically sufficient to fabricate QCDs down to 1.55 μm. Its potential has been demonstrated by the fabrication of short-wavelength quantum cascade lasers.[9] We therefore take advantage of this material and present here three InGaAs/AlAsSb QCDs detecting down to 2.14 μm (0.58 eV) at room temperature.

The basic idea of the QCD is to achieve—via illumination—vertical electron transport along the growth axis. The design used for these QCDs is based on the approach of Graf *et al.*,[5] and is illustrated by the schematic conduction band diagram shown in Fig. 1. The thick quantum well (QW) A is degenerately n-doped in order to populate its ground state A_1. By absorption of a photon with energy $A_1 \rightarrow A_2$, these electrons are lifted into the excited state A_2. From there, they either fall back to A_1 or tunnel to the adjacent state B_1 and "cascade" through C_1, etc., to the ground state A_1' of the following period, thereby generating the desired vertical transport. Using resonant tunneling between A_2 and B_1 allows us to separate the two active QWs by a relatively thick tunnel barrier; this should ideally result in a high resistivity without degrading the electron extraction efficiency from A_2 to A_1'.

For the design, self-consistent Schrödinger-Poisson calculations were performed using the material parameters presented in Ref. 8. Nonparabolicity was taken into account through an energy-dependent effective mass. Based on these calculations, three structures were grown: 3392 and 3505 with a nominal peak detection energy E_p=573 meV (2.16 μm) and 3394 with a nominal peak detection energy E_p=762 meV (1.63 μm). The layer sequences of one active region period are listed in Table I. All samples were grown by molecular beam epitaxy on a semi-insulating InP substrate and consist of a 600 nm thick InGaAs lower contact layer, 20 repetitions of the active region period, and a 200 nm thick InGaAs upper contact layer. The n-type doping density is 2×10^{18} cm^{-3} for the thickest QW of the active region; for the two contact layers, it is listed in Table I. All other layers are nominally undoped. The overall composition and thickness of the active region were confirmed by x-ray diffraction measurements.

The samples were processed into square mesas with a side length of 200 μm using standard photolithography and chemical wet etching. A Ti/Ge/Au/Ti/Au (2/25/50/10/250 nm) metalization deposited by E-gun evaporation on the mesas served as top contact whereas the

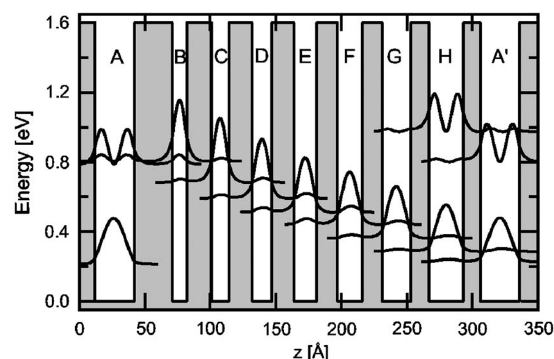

FIG. 1. Band structure of one period of 3392 showing the moduli squared of the relevant wave functions. In the text, ground states and first excited states are identified by the indices 1 and 2, respectively.

[a]Electronic mail: fabrizio.giorgetta@unine.ch

TABLE I. Layer sequences for one period of each sample starting with the thickest QW. InGaAs QW (w) and AlAsSb barrier (b) thicknesses are given in angstroms. E_p is the measured peak responsivity energy at 300 K and n_b is the contact layer doping density.

	E_p (eV)	w	b	w	b	w	b	w	b	w	b	w	b	w	b	w	b	w	b	w	b	n_b (cm^{-3})
3392	0.51	30	26	11	19	13	18	15	17	17	16	19	15	22	14	26	13	⋯	⋯	⋯	⋯	8×10^{18}
3505	0.51	30	24	11	19	13	18	15	17	17	16	19	18	22	20	26	26	⋯	⋯	⋯	⋯	5×10^{17}
3394	0.58	23.4	30	7	25	8	22	9	21	10	20	12	19	14	17	16	16	18	15	20	13	8×10^{18}

etched and metalized surrounding area acted as bottom contact. To couple light into the active region, a 45° facet was polished. The samples were then soldered to a copper submount and wire bonded according to the schematic drawing in the inset of Fig. 2. For spectral and electrical testing, the submount was placed into a liquid He flow cryostat.

For spectral photoresponse measurements, the sample was illuminated with the glowbar of a Fourier transform infrared spectrometer. Without applying an external voltage bias, the current flow between the top and bottom contact was amplified with an SR570 current amplifier and fed back into the spectrometer. The peak responsivity $\mathcal{R}_p$ was then obtained using

$$I=\frac{T}{2}\mathcal{R}_p\int_{-\infty}^{\infty}\tilde{\mathcal{R}}(\lambda)W(\lambda)d\lambda, \qquad (1)$$

where I is the photocurrent of the device illuminated by the spectrometer glowbar measured with an optical chopper and a lock-in amplifier, $T=0.7$ is the transmission coefficient across the 45° facet, $W(\lambda)$ is the glowbar's spectral intensity on the detector surface measured with a thermopile detector, and $\tilde{\mathcal{R}}(\lambda)$ is the detector's spectral photocurrent divided by $W(\lambda)$ and normalized to unity at the peak detection energy. The factor 2 takes into account that the measurements where done with unpolarized light, whereas QWIP responsivities are generally given for TM polarized light.

Figure 2 shows the responsivity spectra of all three samples at 300 K. The responsivity of 3392 peaks at 505 meV (1.53 mA/W) and has a full width at half maximum (FWHM) of 72 meV; for 3394 it peaks at 580 meV (0.32 mA/W) and has a FWHM of 156 meV. Compared to the simulated $A_1\rightarrow A_2$ transition energies of 573 and 762 meV, respectively, the measured values are 12% lower for sample 3392 and even 24% lower for sample 3394. This large discrepancy is a consequence of partly intermixed QW/

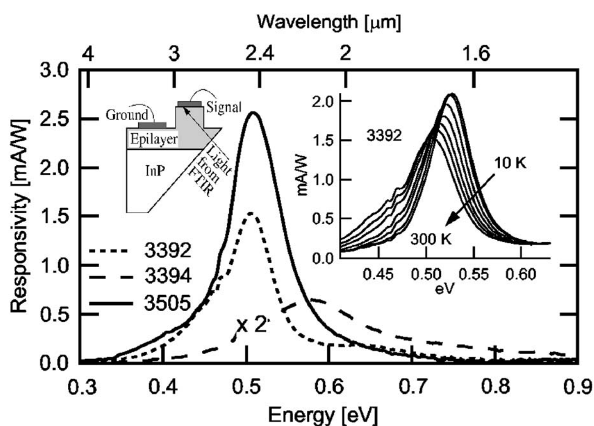

FIG. 2. Responsivities at 300 K. Left inset: schema of a sample processed for responsivity measurements. Right inset: temperature dependence of the responsivity for 3392.

barrier interfaces leading to trapezoidally distorted QWs and thus to a reduced transition energy due to the lifted ground state.[10] Since 3394 contains a considerably thinner active QW, this hypothesis also explains its larger deviation. In addition, simulations of eigenstates lying up to 1.5 eV above the conduction band minimum are considerably affected by uncertainties of the nonparabolicity. Finally, QWs with a thickness of below 1 nm violate one main assumption of the envelope function formalism used in the simulations, namely, that the envelope function varies slowly at the scale of the host material unit cell. This will lead to additional errors in the simulation.

For samples 3392 and 3394, a high energy shoulder is present at 655 and 824 meV, respectively. According to the simulations, this feature has its origin in the $A_1'\rightarrow H_2$ backward transition. To suppress this undesired feature, a redo (sample 3505) of 3392 with a thicker barrier between QWs H and A' was grown and processed. As can be seen in Fig. 2, the high-energy shoulder indeed disappeared for 3505. The inset of Fig. 2 shows the temperature dependence of the responsivity for 3392. As expected for ISB transitions,[11] the peak energy redshifts with increasing temperature with −0.08 meV/K. The observed responsivity decrease for increasing temperatures agrees qualitatively with the lower electron population in A_1 and lower escape probability from A_2 at higher temperatures.

The maximal responsivity $\mathcal{R}_p$ of a quantum cascade detector is given by

$$\mathcal{R}_p=\frac{\eta e}{h\nu}\frac{p_e}{p_c N}, \qquad (2)$$

where $h\nu$ is the peak detection energy, e is the electron charge, η is the overall absorption efficiency, p_e is the escape probability, p_c is the capture probability, and N is the number of periods. For sample 3392, the absorption efficiency for TM polarized light was measured to be $\eta=3.1\%$ for one double pass. With $h\nu\propto E_p=505$ meV and $N=20$, a photovoltaic gain of $p_e/p_c=0.5$ is obtained. As in QCDs p_c is close to unity, the resulting p_e is close to 50%.

The spectral shape of 3505's photocurrent was studied under application of an external field. The top panel of Fig. 3 shows measured spectra of 3505 for different applied fields, as well as a fit consisting of three Lorentzians. The weak black Lorentzian at the lowest energy shows a linear Stark shift of 75 eV/(V/Å), corresponding to the distance between the center of QW A and C (75.5 Å); therefore, it is attributed to the $A_1\rightarrow C_1$ transition. The two Lorentzians at higher energies correspond to the transitions between the ground state A_1 and the coupled states A_2 and B_1; they exhibit an anticrossing if the amplitude of the applied field is modified: in the strongly negative field regime, the low-energy transition is localized in QW B, resulting in a linear Stark shift and a low transition probability from A_1 (which is proportional to

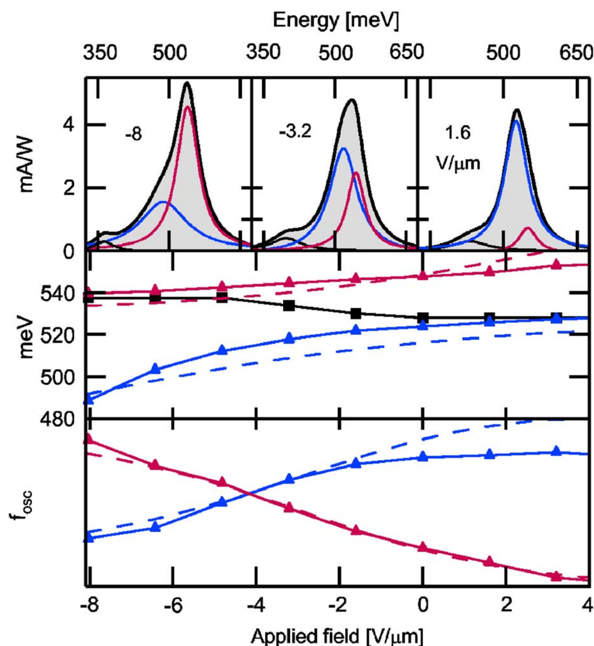

FIG. 3. (Color online) Responsivities of 3505 at 10 K for different applied fields. Top: measured spectra (grey fill) and fits (black thick line) consisting of three Lorentzians (black, blue, and red thin lines) at −8, −3.2, and 1 V/μm. Center: measured peak energies of the low- and high-energy Lorentzians (blue and red triangles), corresponding simulation results (blue and red dashed line), and global peak responsivity energy (black squares). Bottom: amplitude of the fitted Lorentzians (blue and red triangles) and simulated squared dipole matrix elements (blue and red dashed lines).

the oscillator strength f). In contrast, the high energy transition is localized in QW A, does not shift, and has a high f. For low fields, both wave functions are localized in QWs A and B and have a nonlinear Stark shift and comparable oscillator strength. For strongly positive fields, finally, the low energy wave function is localized in QW A, does not Stark shift, and has a high f, whereas the high energy wave function is localized in QW B and exhibits a linear Stark shift and a low f. As seen in the center panel of Fig. 3, the measured peak detection energies of the two Lorentzians correspond well to the ones obtained by band structure simulations. The lower panel of Fig. 3 compares the amplitude of the measured Lorentzians with the simulated squared dipole matrix elements, again showing good qualitative agreement between experiment and simulation. The somewhat counterintuitive shift of the overall peak responsivity, also shown in the center panel of Fig. 3, is caused by anticrossing; its direction is opposite to the $A_1 \rightarrow C_1$ Stark shift. The observation of anticrossing shows that a very good alignment between A_2 and B_1 was achieved.

Figure 4 shows the current-voltage curve of sample 3505 under 300 K background and glowbar illumination for different temperatures. The graph clearly demonstrates the photovoltaic nature of the detector. Transport calculations[12] showed that the dark current is dominated by intercascade transitions from the ground state A_1. At room temperature, the $A_1 \rightarrow C_1$ transition has the highest rate; at lower temperatures, transitions from A_1 towards the lower lying wave functions D_1, E_1, and F_1 become more important, and at 5 K, the dark current has its origin mostly in the $A_1 \rightarrow G_1$ transition. Based on the device resistance R_0 measured under dark conditions and the measured peak responsivity $\mathcal{R}_p$, 3505's

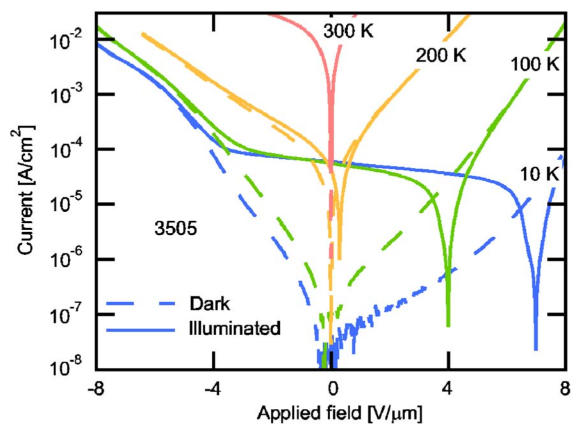

Johnson noise limited detectivity was calculated to be 7.8 $\times 10^{11}$ Jones at 10 K and 1.2×10^8 Jones at 300 K.

In conclusion, room temperature short-wavelength $In_{0.53}Ga_{0.47}As/AlAs_{0.56}Sb_{0.44}$ QCDs were demonstrated. Two of them detected near-infrared radiation with a photon energy of 505 meV (2.46 μm) whereas the third one was sensitive at 580 meV (2.14 μm). The peak responsivity of the 505 meV QCD was 2.57 mA/W at 300 K. For 3505, anticrossing of two quantized electron levels was observed in the photoresponse when applying different biases, demonstrating both good material quality and a high confidence level of the band structure simulations. Future work should concentrate on increasing the detectivity by augmenting the device resistance; this could be achieved by designing larger barriers in the first half of the cascade, where the thermally activated electron transfer is dominant.

The authors thank the Professorship Program and the National Center of Competence in Research "Quantum Photonics," both of the Swiss National Science Foundation, for their financial support. Furthermore, the authors thank L. Kirste for x-ray characterization.

[1] H. Schneider, P. Koidl, F. Fuchs, B. Dischler, K. Schwarz, and J. Ralston, Semicond. Sci. Technol. **6**, C120 (1991).
[2] B. F. Levine, K. K. Choi, C. G. Bethea, J. Walker, and R. J. Malik, Appl. Phys. Lett. **50**, 1092 (1987).
[3] L. Gendron, M. Carras, A. Huynh, V. Ortiz, C. Koeniguer, and V. Berger, Appl. Phys. Lett. **85**, 2824 (2004).
[4] L. Gendron, C. Koeniguer, V. Berger, and X. Marcadet, Appl. Phys. Lett. **86**, 121116 (2005).
[5] M. Graf, N. Hoyler, M. Giovannini, J. Faist, and D. Hofstetter, Appl. Phys. Lett. **88**, 241118 (2006).
[6] F. R. Giorgetta, E. Baumann, M. Graf, L. Ajili, N. Hoyler, M. Giovannini, J. Faist, D. Hofstetter, P. Krotz, and G. Sonnabend, Appl. Phys. Lett. **90**, 231111 (2007).
[7] M. Graf, G. Scalari, D. Hofstetter, J. Faist, H. Beere, E. Linfield, D. Ritchie, and G. Davies, Appl. Phys. Lett. **84**, 475 (2004).
[8] N. Georgiev and T. Mozume, J. Appl. Phys. **89**, 1064 (2001).
[9] Q. K. Yang, C. Manz, W. Bronner, K. Kohler, and J. Wagner, Appl. Phys. Lett. **88**, 121127 (2006).
[10] P. Cristea, Y. Fedoryshyn, J. F. Holzman, F. Robin, H. Jackel, E. Muller, and J. Faist, J. Appl. Phys. **100**, 116104 (2006).
[11] D. C. Larrabee, G. A. Khodaparast, J. Kono, K. Ueda, Y. Nakajima, M. Nakai, S. Sasa, M. Inoue, K. I. Kolokolov, J. Li, and C. Z. Ning, Appl. Phys. Lett. **83**, 3936 (2003).
[12] C. Koeniguer, G. Dubois, A. Gomez, and V. Berger, Phys. Rev. B **74**, 235325 (2006).